Inorg. Chem. **2005**, *44*, 3827–3836

Single-Molecule Magnets: High-Field Electron Paramagnetic Resonance Evaluation of the Single-Ion Zero-Field Interaction in a $Zn^{II}_3Ni^{II}$ Complex

En-Che Yang,[†] Cem Kirman,[‡] Jon Lawrence,[‡] Lev N. Zakharov,[†] Arnold L. Rheingold,[†] Stephen Hill,*[,‡] and David N. Hendrickson*[,†]

Department of Physics, University of Florida, Gainesville, Florida 32611-8440, and Department of Chemistry and Biochemistry, University of California at San Diego, La Jolla, California 92093-0358

Received December 16, 2004

High-field electron paramagnetic resonance spectra were collected at several frequencies for a single crystal of $[Zn_{3.91}Ni_{0.09}(hmp)_4(dmb)_4Cl_4]$ (**1**), where dmb is 3,3-dimethyl-1-butanol and hmp^- is the monoanion of 2-hydroxymethylpyridine. This crystal is isostructural to $[Ni_4(hmp)_4(dmb)_4Cl_4]$ (**2**), which has been characterized to be a single-molecule magnet (SMM) with fast quantum tunneling of its magnetization (QTM). The single Ni^{II} ion zero-field-splitting (zfs) parameters D_i [$= -5.30(5)$ cm^{-1}] and E_i [$= \pm 1.20(2)$ cm^{-1}] in the doped complex **1** were evaluated by rotation of a crystal in three planes. The easy-axes of magnetization associated with the single-ion zfs interactions were also found to be tilted 15° away from the crystallographic *c* direction. This inclination provides a possible explanation for the fast QTM observed for complex **2**. The single-ion zfs parameters are then related to the zfs parameters for the Ni_4 molecule by irreducible tensor methods to give $D = -0.69$ cm^{-1} for the $S = 4$ ground state of the SMM, where the axial zfs interaction is given by $D\hat{S}_z^2$.

Introduction

Single-molecule magnets (SMMs) are molecular nanomagnets that exhibit magnetization hysteresis below their blocking temperatures.[1−23] Several quantum effects have been observed in the magnetization dynamics of SMMs, such as tunneling of the direction of magnetization,[4,5] quantum phase interference,[6] and spin parity effects.[6,7] It has, therefore, been suggested that SMMs could some day be employed as the smallest magnetic memory unit[2,3] or in quantum computational devices.[8−10]

Polynuclear complexes of several first-row transition metals have been reported to function as SMMs, manganese complexes being the most prevalent.[11] However, SMMs have also been identified with Fe,[12] V,[13] Cr,[14] and Ni.[15−17] In this paper, we focus on Ni^{II}_4 SMMs of the composition $[Ni_4(hmp)_4(ROH)_4Cl_4]\cdot S$, where hmp^- is the monoanion of 2-hydroxymethylpyridine, R is some substituent, and S is a

* Author to whom correspondence should be addressed. E-mail: dhendrickson@ucsd.edu (D.N.H.) and hill@phys.ufl.edu (S.H.).
[†] University of California at San Diego.
[‡] University of Florida.

(1) Christou, G.; Gatteschi, D.; Hendrickson, D. N.; Sessoli, R. *MRS Bull.* **2000**, *25* (11), 66−71.
(2) Sessoli, R.; Tsai, H. L.; Schake, A. R.; Wang, S. Y.; Vincent, J. B.; Folting, K.; Gatteschi, D.; Christou, G.; Hendrickson, D. N. *J. Am. Chem. Soc.* **1993**, *115* (5), 1804−1816.
(3) Sessoli, R.; Gatteschi, D.; Caneschi, A.; Novak, M. A. *Nature* **1993**, *365* (6442), 141−143.
(4) Friedman, J. R.; Sarachik, M. P.; Tejada, J.; Ziolo, R. *Phys. Rev. Lett.* **1996**, *76* (20), 3830−3833.
(5) Thomas, L.; Lionti, F.; Ballou, R.; Gatteschi, D.; Sessoli, R.; Barbara, B. *Nature* **1996**, *383* (6596), 145−147.
(6) Wernsdorfer, W.; Sessoli, R. *Science* **1999**, *284* (5411), 133−135.
(7) Wernsdorfer, W.; Bhaduri, S.; Boskovic, C.; Christou, G.; Hendrickson, D. N. *Phys. Rev. B: Condens. Matter* **2002**, *65* (18), 180403.
(8) Leuenberger, M. N.; Loss, D. *Nature* **2001**, *410* (6830), 789−793.
(9) Zhou, B.; Tao, R. B.; Shen, S. Q.; Liang, J. Q. *Phys. Rev. A: At., Mol., Opt. Phys.* **2002**, *66* (1).
(10) Hill, S.; Edwards, R. S.; Aliaga-Alcalde, N.; Christou, G. *Science* **2003**, *302* (5647), *1015−1018*.
(11) Wernsdorfer, W.; Aliaga-Alcalde, N.; Hendrickson, D. N.; Christou, G. *Nature* **2002**, *416* (6879), 406−409. (b) Soler, M.; Wernsdorfer, W.; Folting, K.; Pink, M.; Christou, G. *J. Am. Chem. Soc.* **2004**, *126* (7), 2156−2165. (c) Sanudo, E. C.; Brechin, E. K.; Boskovic, C.; Wernsdorfer, W.; Yoo, J.; Yamaguchi, A.; Concolino, T. R.; Abboud, K. A.; Rheingold, A. L.; Ishimoto, H.; Hendrickson, D. N.; Christou, G. *Polyhedron* **2003**, *22* (14−17), 2267−2271. (d) Brechin, E. K.; Boskovic, C.; Wernsdorfer, W.; Yoo, J.; Yamaguchi, A.; Sanudo, E. C.; Concolino, T. R.; Rheingold, A. L.; Ishimoto, H.; Hendrickson, D. N.; Christou, G. *J. Am. Chem. Soc.* **2002**, *124* (33), 9710−9711. (e) Yoo, J.; Yamaguchi, A.; Nakano, M.; Krzystek, J.; Streib, W. E.; Brunel, L. C.; Ishimoto, H.; Christou, G.; Hendrickson, D. N. *Inorg. Chem.* **2001**, *40* (18), 4604−4616. (f) Aubin, S. M. J.; Wemple, M. W.; Adams, D. M.; Tsai, H. L.; Christou, G.; Hendrickson, D. N. *J. Am. Chem. Soc.* **1996**, *118* (33), 7746−7754. (g) Yoo, J.; Brechin, E. K.; Yamaguchi, A.; Nakano, M.; Huffman, J. C.; Maniero, A. L.; Brunel, L. C.; Awaga, K.; Ishimoto, H.; Christou, G.; Hendrickson, D. N. *Inorg. Chem.* **2000**, *39* (16), 3615−3623.

10.1021/ic0482279 CCC: $30.25
Published on Web 04/23/2005

solvate molecule. As we previously communicated,[16,18] these Ni^{II}_4 SMMs exhibit magnetization versus magnetic field hysteresis loops that indicate the presence of a relatively fast rate of magnetization tunneling (a small coercive field in the loop) and, in certain cases, the presence of an exchange bias.[11,16] Detailed measurements have been carried out in order to determine the origin of the fast magnetization tunneling; the results will be given in several papers, including this one.

The three requirements for a molecule to be a SMM are (1) a relatively large spin S for the ground state; (2) an appreciable negative magnetoanisotropy, that is, a dominant zero-field splitting (zfs) term, $D\hat{S}_z^2$ ($D < 0$), in the spin Hamiltonian; and (3) not too large a value for the tunnel splitting of the ground state (caused by terms in the spin Hamiltonian that do not commute with $\hat{S}_z$). The large spin and negative magnetoanisotropy determine the magnitude of the thermodynamic barrier for classical thermal activation, leading to reversal of the direction of magnetization for a molecule. It is important to emphasize that, even if a particular complex has a large barrier for magnetization reversal, it may not function as a SMM if the complex has a very fast rate of quantum tunneling of the direction of its magnetization. The Ni^{II}_4 SMMs have a spin $S = 4$ ground state and a negative magnetoanisotropy.[16,18,19] The question is, why do they exhibit a fast rate of magnetization tunneling? In this and following papers, we will answer this question.[19,20]

The D value for a SMM results largely from the single-ion D_i values for each of the metal ions in the molecule. The inter-ion magnetic exchange interactions in a Ni^{II}_4 complex give rise to a ground state with an axial zfs interaction $D\hat{S}_z^2$ that results from a projection of the single-ion zfs interactions at each of the four Ni^{II} ions. D values for Ni^{II} complexes have been found to be both positive and negative.[21] Thus, the first question arising concerns the sign of the axial zfs parameter for the individual Ni^{II} ions and whether a positive single-ion D_i value could project a negative D value for the $S = 4$ ground state of a Ni_4 SMM. To answer this, we have prepared single crystals of $[Zn_{3.91}Ni_{0.09}(hmp)_4(dmb)_4Cl_4]$ (**1**), where dmb is 3,3-dimethyl-1-butanol. High-field electron paramagnetic resonance (HFEPR) experiments have then been carried out on a single crystal of this doped complex in order to determine the single-ion spin zfs parameters (D_i, E_i, g, etc.) at each of the four possible Ni^{II} sites for a $[Zn_3Ni(hmp)_4(dmb)_4Cl_4]$ molecule doped into a $[Zn_4(hmp)_4(dmb)_4Cl_4]$ crystal. We note that a similar methodology has recently been employed by Pardi et al., for a one-dimensional Ni^{II} haldane chain system.[22] However, to the best of our knowledge, this is the first such study by HFEPR for a SMM. The single-crystal measurements further enable us to determine the orientations of the principal magnetic axes at each of the Ni^{II} sites and to show how the D value of the $S = 4$ Ni^{II}_4 SMM results from the D_i and E_i values ($i = 1-4$) for the four exchange-coupled Ni^{II} ions. Finally, we investigate how the single-ion spin-Hamiltonian parameters affect the thermodynamic barrier for magnetization reversal as well as the tunnel splitting for the Ni_4 SMM.

Experimental Section

Synthetic Procedure. All operations were carried out in air. All reagents were purchased from Aldrich.

$[Zn_{3.91}Ni_{0.09}(hmp)_4(dmb)_4Cl_4]$ (1). 1.23 g (9 mmol) of $ZnCl_2$, 0.24 g (1 mmol) of $NiCl_2 \cdot 6H_2O$, 1.09 g (10 mmol) of hmpH (2-hydroxymethylpyridine), and 0.54 g of NaOMe (10 mmol) were dissolved in 80 mL of MeOH and refluxed for 30 min. The resulting solution was then filtered and left at room temperature for over 1 week. Pale-green prism-shaped crystals were then isolated. A total of 1.6 g of these pale-green crystals were collected by repeating the above procedures several times. The crystals were then suspended in 30 g of 3,3-dimethyl-1-butanol (dmb), and 40 mL of methylene chloride was added to dissolve the solids. The resulting solution was filtered and kept in an ambient environment for slow evaporation. Pale-green bipyramidal-shaped crystals formed after 2 weeks with an overall yield of 10%. Anal. Calcd for **1**, $C_{48}H_{80}Cl_4N_4O_8Zn_{3.91}Ni_{0.09}$: C, 46.34; H, 6.48; N, 4.50. Found: C, 46.96; H, 6.55; N, 4.15. Selected IR data (KBr, cm^{-1}): 3310 (br, s), 2960 (s), 2860 (s), 1600 (s), 1570 (s), 1480 (s), 1440 (s), 1400 (s), 1370 (s), 1290 (s), 1250 (m), 1220 (m), 1160 (s), 1080 (s), 1050 (s), 997 (s), 974 (s), 920 (m), 889 (w), 870 (w), 839 (m), 818 (s), 754 (s), 731 (s), 702 (w), 644 (s), 496 (m), 463 (m).

X-ray Structure Determination. Diffraction data for a crystal of $[Zn_{3.91}Ni_{0.09}(hmp)_4(dmb)_4Cl_4]$ were collected at 100(2) K with a Bruker Smart Apex CCD diffractometer equipped with Mo Kα radiation ($\lambda = 0.710\,73$ Å). SADABS absorption correction was applied. The structure was solved by direct methods and refined on F^2 by a full-matrix least-squares procedure (SHELXTL, version 6.10, Bruker AXS, Inc., 2000). All atoms except the hydrogen were refined anisotropically. Hydrogen atoms were placed in calculated idealized positions. In the refinement, all metal atoms in the structure were treated as the Zn atom. Crystallographic data and details of the X-ray study are given in Table 1.

HFEPR. A good-sized crystal [approximate dimensions: 1.5×1.5 mm^2 square base; 2 mm height] of complex **1** was selected to perform the single-crystal HFEPR measurements. The orientation

(12) Gatteschi, D.; Sessoli, R.; Cornia, A. *Chem. Commun.* **2000**, No. 9, 725−732.
(13) Castro, S. L.; Sun, Z. M.; Grant, C. M.; Bollinger, J. C.; Hendrickson, D. N.; Christou, G. *J. Am. Chem. Soc.* **1998**, *120* (10), 2365−2375.
(14) Piligkos, S.; Collison, D.; Oganesyan, V. S.; Rajaraman, G.; Timco, G. A.; Thomson, A. J.; Winpenny, R. E. P.; McInnes, E. J. L. *Phys. Rev. B: Condens. Matter* **2004**, *69* (13), 134424.
(15) Moragues-Canovas, M.; Helliwell, M.; Ricard, L.; Riviere, E.; Wernsdorfer, W.; Brechin, E.; Mallah, T. *Eur. J. Inorg. Chem.* **2004**, No. 11, 2219−2222.
(16) Yang, E. C.; Wernsdorfer, W.; Hill, S.; Edwards, R. S.; Nakano, M.; Maccagnano, S.; Zakharov, L. N.; Rheingold, A. L.; Christou, G.; Hendrickson, D. N. *Polyhedron* **2003**, *22* (14−17), 1727−1733.
(17) Andres, H.; Basler, R.; Blake, A. J.; Cadiou, C.; Chaboussant, G.; Grant, C. M.; Gudel, H. U.; Murrie, M.; Parsons, S.; Paulsen, C.; Semadini, F.; Villar, V.; Wernsdorfer, W.; Winpenny, R. E. P. *Chem.—Eur. J.* **2002**, *8* (21), 4867−4876.
(18) Edwards, R. S.; Maccagnano, S.; Yang, E.-C.; Hill, S.; Wernsdorfer, W.; Hendrickson, D.; Christou, G. *J. Appl. Phys.* **2003**, *93* (10), 7807−7809.
(19) Lawrence, J.; Yang, E.-C.; Edwards, R. S.; Olmstead, M. M.; Ramsey, C.; Dalal, N.; Gantzel, P. K.; Hill, S.; Hendrickson, D. N. Submitted for publication.
(20) Yang, E.-C.; Wernsdorfer, W.; Zakharov, L. N.; Yamaguchi, A.; Isidro, R. M.; Lu, G.-D.; Rheingold, A. L.; Ishimoto, H.; Hendrickson, D. N., Submitted for publication.
(21) Bencini, A.; Gatteschi, D. *Trans. Met. Chem.* **1980**, *8*, 1−178.
(22) Pardi, L. A.; Hassan, A. K.; Hulsbergen, F. B.; Reedijk, J.; Spek, A. L.; Brunel, L.-C. *Inorg. Chem.* **2000**, *39* (2), 159−164.
(23) Mola, M.; Hill, S.; Goy, P.; Gross, M. *Rev. Sci. Instrum.* **2000**, *71* (1), 186−200.

Table 1. Crystallographic Data for $[Zn_{3.91}Ni_{0.09}(hmp)_4(dmb)_4Cl_4]$ (complex **1**)

formula[a]	$C_{48}H_{80}Cl_4N_4O_8M$
fw, g/mol	1244.44
temp	100(2) K
space group	$I4_1/a$
a, Å	12.9165(4)
b, Å	12.9165(4)
c, Å	35.038(2)
$\alpha = \beta = \gamma$	90°
vol	5845.7(4) Å^3
Z, Z′	4, 0.25
F(000)	2592
density calcd	1.414 g cm^{-3}
abs coeff	1.854 mm^{-1}
abs correction	SADABS
transmission max/min	0.7684/0.6062
reflns, measured	18318
reflns, independent	3355 [Rint = 0.0181]
data/restrains/params	3355/0/234
GOF on F^2	1.055
R indices [I $>2\sigma$(I)]	R1 = 0.0214, wR2 = 0.0546
R indices (all data)	R1 = 0.0233, wR2 = 0.0554

[a] M represents Zn or Ni.

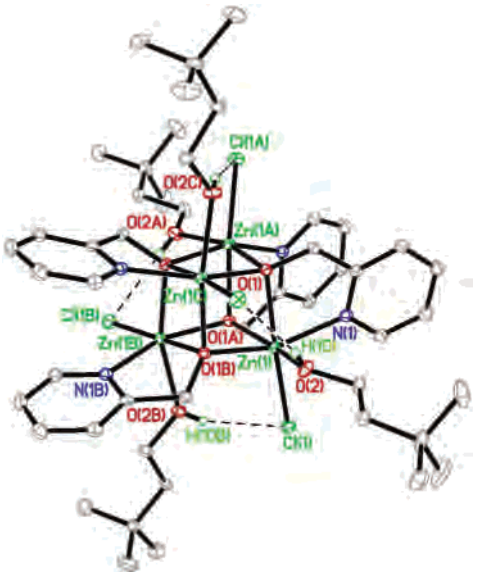

Figure 1. ORTEP plot of $[Zn_{3.91}Ni_{0.09}(hmp)_4(dmb)_4Cl_4]$ at the 30% probability level. Intramolecular O−H···Cl H-bonds are shown by dashed lines.

of the crystal was confirmed by determining crystal face indices on the basis of X-ray diffractometry prior to the HFEPR measurements. The HFEPR spectrometer is equipped for conducting high-sensitivity angle-dependent cavity perturbation measurements over a broad frequency range (40−350 GHz) and in the presence of a strong magnetic field (up to 17 T). A millimeter-wave vector network analyzer acts as a continuously tunable microwave source and phase-sensitive detector (8−350 GHz), enabling simultaneous measurements of the complex cavity parameters at a rapid repetition rate (∼10 kHz). A pumped ^{4}He cryostat system was utilized to control the temperature of the experiment. A detailed description of the spectrometer can be found in the literature.[23,24]

Inductively Coupled Plasma-Optical Emission Spectrometry (ICPOES). A Perkin-Elmer Optima 3000 DV ICPOES system with axially viewed plasmas was employed. The operation process of this system is described elsewhere.[25] The wavelengths of 213.86 nm for Zn and 231.60 nm for Ni were used to identify these elements. A quantity of 0.0375 g of complex **1** was diluted 118.5 times in 1% HNO_3 solution, and this solution was further diluted 160 times. The highest dilution factors were 196 ppb of Ni and 8460 ppb of Zn. Therefore, a molar ratio of Zn/Ni= 97.74: 2.26 was obtained.

Results and Discussion

Preparation of the Ni^{II}-Doped Zn^{II}_4 Complex. The goal was to prepare a crystal that is isostructural with $[Ni_4(hmp)_4(dmb)_4Cl_4]$ (complex **2**), but where the Ni^{II} ions are doped into a diamagnetic lattice. Through separate experiments, it was known that $[Zn_4(hmp)_4(dmb)_4Cl_4]$ (complex **3**) could be prepared, where the Zn^{II} ions obviously do not have unpaired electrons. Consequently, we prepared faintly green $[Zn_{3.91}Ni_{0.09}(hmp)_4(dmb)_4Cl_4]$ (complex **1**) crystals. A relatively precise value of the Zn/Ni ratio in the crystals was obtained by ICPOES spectra, which gave Zn/Ni = 97.74: 2.26%. Provided that there is little difference in the heats of formation for either the Zn_4 or Ni_4 complexes, the Ni^{II} ions in $[Zn_{3.91}Ni_{0.09}(hmp)_4(dmb)_4Cl_4]$ should be randomly distributed in the crystal. On the basis of this assumption, it is a relatively straightforward exercise to compute the probabilities for the formation of the Zn_4, Zn_3Ni, Zn_2Ni_2, $ZnNi_3$, and Ni_4 complexes, as a function *x*, in the formula $[Zn_{4x}Ni_{4-4x}(hmp)_4(dmb)_4Cl_4]$ (see Figure S1 in the Supporting Information). When $x = 0.977$, it is found that the Zn_4 and Zn_3Ni species make up 91% and 8% of the total population, respectively. Thus, the doped crystal is comprised of some $S = 1$ $[Zn_3Ni_1(hmp)_4(dmb)_4Cl_4]$ complexes doped randomly into a diamagnetic Zn_4 host crystal. Because the Ni^{II} ions are ferromagnetically coupled with each other in the Zn_2Ni_2, $ZnNi_3$, and Ni_4 complexes, one would expect ground states of $S = 2$, 3, and 4, respectively, for these three possibilities. The absence of significant HFEPR peak intensities for these spin values confirms that the predominant paramagnetic species present in the crystal is the Zn_3Ni complex.

X-ray Structure of $[Zn_{3.91}Ni_{0.09}(hmp)_4(dmb)_4Cl_4]$. Like the analogous Ni_4 complex **2**, $[Zn_{3.91}Ni_{0.09}(hmp)_4(dmb)_4Cl_4]$ (**1**) crystallizes in the tetragonal $I4_1/a$ space group with four molecules in the unit cell without solvate molecules (see Table 1). Figure 1 shows the ORTEP plot of complex **1**. If each metal atom is treated as a Zn atom, molecule **1** has S_4 site symmetry with the metal ions occupying the alternating corners of the distorted cubane core. In addition to the chelating hmp^- ligands, the central M_4O_4 core (M = Ni or Zn) is bonded to four Cl^- anions and four 3,3-dimethyl-1-butanol ligands. A comparison of bond lengths and angles between complexes **1** and **2** is given in Table 2. As expected, the metal−ligand atom bond distances for the $Zn_{3.91}Ni_{0.09}$ complex are longer by 0.02−0.11 Å than those for the Ni_4 complex. The Ni−Cl bond length is, however, 0.002 Å longer than the Zn−Cl distance. The bond angles characterizing the Ni_4 and $Zn_{3.91}Ni_{0.09}$ complexes are similar. It seems reasonable that, in the crystal for complex **1**, the few Zn_3Ni complexes should be randomly distributed among the Zn_4 complexes. Also, it is clear that any spin-Hamiltonian

(24) Takahashi, S.; Hill, S. *Rev. Sci. Instrum.* **2005**, *76*, 023114.
(25) Cai, Q.; Luo, N.; Chen, F.; Yang, Z. *Anal. Sci.* **2001**, *17*, i853.

Table 2. Comparison of Selected Bond Lengths (Å) and Bond Angles (deg) for Complexes **1** and **2**[a]

	complex **2**	complex **1**
M(1)−O(1)#1	2.0510(13)	2.0709(9)
M(1)−O(1)#2	2.1018(13)	2.1245(9)
M(1)−O(1)	2.0374(13)	2.1338(9)
M(1)−O(2)	2.0893(14)	2.1972(10)
M(1)−N(1)	2.0648(16)	2.1246(11)
M(1)−Cl(1)	2.3593(5)	2.3377(3)
O(1)#1−M(1)−O(1)#2	80.73(5)	81.02(4)
O(1)#1−M(1)−N(1)	161.13(6)	156.35(4)
O(1)#2−M(1)−N(1)	101.79(5)	103.41(4)
O(1)#1−M(1)−O(1)	82.29(4)	80.80(4)
O(1)#2−M(1)−O(1)	80.10(5)	79.92(4)
N(1)−M(1)−O(1)	79.78(6)	77.22(4)
O(1)#1−M(1)−O(2)	85.13(5)	83.07(4)
O(1)#2−M(1)−O(2)	165.09(5)	162.74(4)
N(1)−M(1)−O(2)	90.09(6)	88.63(4)
O(1)−M(1)−O(2)	93.38(5)	90.97(4)
O(1)#1−M(1)−Cl(1)	100.57(4)	103.65(3)
O(1)#2−M(1)−Cl(1)	96.00(4)	97.71(3)
N(1)−M(1)−Cl(1)	97.76(5)	98.79(3)
O(2)−M(1)−Cl(1)	91.21(4)	92.52(3)
O(1)−M(1)−Cl(1)	174.79(4)	174.64(3)

[a] M represents Zn or Ni in **1** and Ni in **2**.

parameters characterized for the Ni^{II} ions in complex **1** would be quite close in value to those found for the Ni^{II} single ions in the Ni_4 crystal.

Crystals of **1** and **2** have the same space group and the same morphology, that is, that of a rectangular-based bipyramid. The relationship between the unit cell directions and the crystal faces can be found in the Supporting Information (Figure S2). The *c* axis coincides with the bottom-to-top diagonal direction of the crystal, whereas the *a* and *b* axes are aligned with the edges of the rectangular base. The magnetic easy axis for complex **2** (the Ni_4 SMM) is found to be along the crystallographic *c* axis.

HFEPR Spectroscopy of $[Zn_{3.91}Ni_{0.09}(hmp)_4(dmb)_4Cl_4]$ (1). There are several reasons why we selected the doped crystal of complex **1** for single-crystal HFEPR experiments. First, the orientation of the crystal lattice relative to the faces of a crystal can easily be deduced. Second, the *tert*-butyl groups on the dmb ligand provide considerable insulation between molecules in this complex. Therefore, intermolecular magnetic exchange interactions are minimized, as substantiated by the absence of any measurable exchange bias in the magnetization versus magnetic field hysteresis loop for the SMM Ni^{II}_4 complex (**2**).[16,18] Third, there are no solvated molecules in the crystals of complexes **1** and **2**. Disorder associated with any solvate molecules can give broad HFEPR signals, as was seen for the methanol and ethanol analogues of complex **2**.[18,19] Thus, the crystals of complexes **1** and **2** give relatively sharp HFEPR signals, as will be discussed in detail in a later paper.[19]

Before the HFEPR spectra are discussed, it is worthwhile to check how many different metal sites are available for the individual Ni^{II} ions. A stereoview of the molecular packing in the unit cell of complex **1** is shown in Figure 2. At a first glance, it looks like there are two kinds of molecular orientations that are related by a 4-fold rotation axis. Thus, for each kind of cubane, with four Ni^{II} sites available, there appear to be eight different single-ion orientations that need

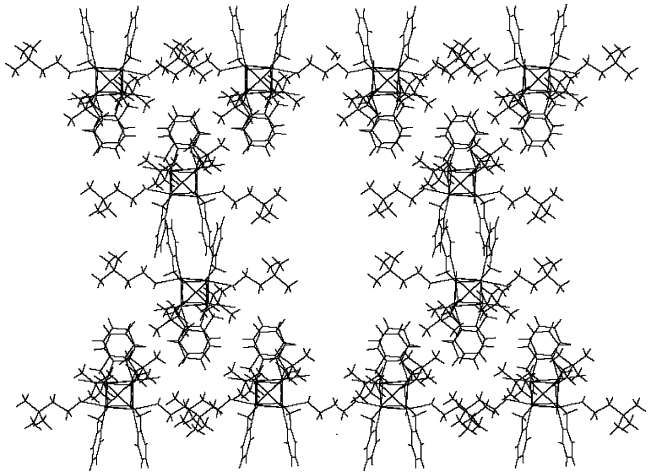

Figure 2. Stereo plot of the molecule packing in $[Zn_{3.91}Ni_{0.09}(hmp)_4(dmb)_4Cl_4]$.

to be accounted for. However, after a closer inspection, it is found that these two molecular orientations are actually related by an inversion operation. Therefore, because of the intrinsic inversion symmetry associated with the operators $D\hat{O}_2^0$ and $E\hat{O}_2^2$ in the spin Hamiltonian, only four different orientations of the Ni^{II} ions need to be considered.

The most direct way to deduce the orientations of the principal magnetic axes associated with the individual Ni^{II} zfs interactions involves measuring the angle dependence of EPR spectra for several different planes of rotation. As will be seen below, such measurements were performed for three carefully chosen rotation planes. However, fits to such data contain many adjustable parameters, for example, the various Ni^{II} spin-Hamiltonian parameters (D_i, E_i, g_i, etc.), the Euler angles that relate the local magnetic axes to the crystallographic axes, and additional Euler angles that take into account minor misalignments between the actual and assumed rotation frames. For this reason, we first set out to estimate the Ni^{II} spin-Hamiltonian parameters via frequency-dependent measurements. Spectra were thus obtained between 58 and 352 GHz with the dc field approximately aligned along the *c* axis of the crystal, as displayed in Figure 3; this orientation was deduced from preliminary angle-dependent data. Because of the 4-fold symmetry of the crystal structure, one may assume that the angles (θ_i) between the magnetic easy axes for the four Ni^{II} ion sites and the applied magnetic field are more or less the same for this field orientation. Thus, the frequency dependence of the spectra should roughly superimpose, with any splittings likely due to small deviations from perfect field alignment along the *c* axis. Indeed, three distinct EPR absorptions are seen in the experimental spectra (see Figure S3 in the Supporting Information). Each EPR absorption consists of several closely spaced peaks, which we believe are mainly due to a slight misalignment of the applied field. However, it is also likely that these splittings are caused by different microenvironments, as has been found for the parent $[Ni(hmp)(dmb)Cl]_4$ system.[18]

Figure 3 displays the frequency dependence of the positions (in field) of the three EPR absorptions. Each data point is located at the center of an absorption, and the error bars

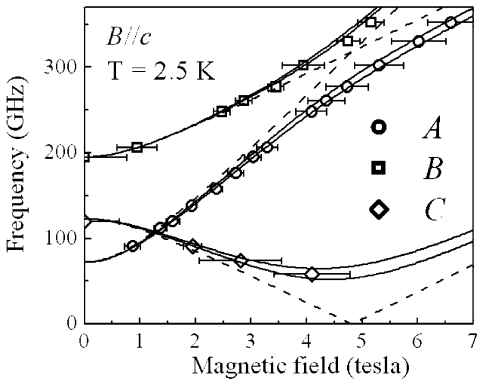

Figure 3. Frequency dependence of the positions (in field) of the three resonance branches. Each point is located at the center of a resonance, and the error bars represent the range over which fine structures are observed. Superimposed on the data are several simulations of the frequency dependence of the resonance positions, obtained by taking difference frequencies between the $2S + 1$ energy levels for $S = 1$, as shown in Figure 4. See the main text for an explanation of the simulations and Figure 4 for the labeling of the various transitions (*A*, *B*, *C*).

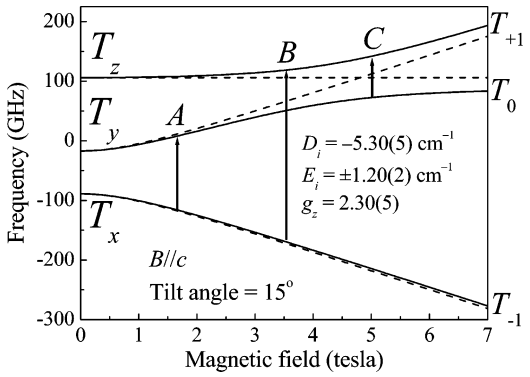

Figure 4. Energy level diagram for $S = 1$, assuming a negative uniaxial D_i parameter. The spin-Hamiltonian parameters, corresponding to the obtained values for $[NiZn_3(hmp)_4(dmb)_4Cl_4]$, are indicated in the figure. The solid curves correspond to the case where the magnetic field is applied parallel to the *c* axis of the crystal [(001) direction]. The dashed curve corresponds to the case where the magnetic field is applied parallel to the local easy axis of one of the Ni^{II} ions. The levels have been labeled in zero-field according to the scheme described in the main text, and the transitions observed in Figure 3 are represented by the vertical arrows.

indicate the range over which the fine-structure peaks are observed. Superimposed on the data are several simulations of the frequency dependence, obtained by taking difference frequencies between the $2S + 1$ energy levels for $S = 1$, as shown in Figure 4. These triplet levels are labeled T_x, T_y, and T_z in zero field, in order of ascending energy; T_z corresponds to the $M_S = 0$ state, whereas T_x and T_y correspond to the symmetric and antisymmetric combinations of the pure $M_S = \pm 1$ states. At high fields, the triplet states are labeled T_{-1}, T_0, and T_{+1} in order of ascending energy; here, the subscripts refer to the spin projection onto the magnetic field quantization axis. Considering all possible transitions between these three levels, one expects three resonance branches (*A*, *B*, and *C*), which extrapolate to three different zero-field offsets (splittings). These offsets are sufficient for estimating D_i and E_i; D_i is responsible for the splitting between the upper $M_S = 0$ state and the $M_S = \pm 1$ doublet; E_i is responsible for the splitting of the $M_S = \pm 1$ states. We note that, to within the experimental uncertainty, single values for D_i and E_i are sufficient for fitting all of the data, as one would expect from the 4-fold symmetry of the molecule.

Estimation of the *g* factor requires knowledge of the field orientation relative to the magnetic axes at the individual Ni^{II} sites. The dashed curves in Figures 3 and 4 have been generated with the same D_i, E_i, and *g* values as the solid curves, but they assume that the single-ion easy axes are aligned with the applied magnetic field. In this situation, one sees that the T_y and T_z states pass right through each other and that resonances *A* and *B* also pass right through each other. On the other hand, the data clearly indicate a level repulsion, which depends very sensitively on the field orientation. Thus, armed with approximate D_i and E_i values, one can adjust the field orientation (equivalent to tilting the single-ion easy axes away from the crystallographic *c* axis) and the *z* component of the *g* factor until the behavior of the *A* and *B* resonances is accurately reproduced. This procedure provides a good first estimate of the tilting of the single-ion easy axes away from the crystallographic *c* axis, that is, $\sim 15°$.

The curves in Figures 3 and 4 were actually generated using the final parameter set determined from the full angle dependence (see below and inset to Figure 4). The two sets of solid curves in Figure 3 illustrate the small effect of the transverse field component for this field orientation. Because we do not yet know the orientations of the hard and medium directions associated with each of the Ni^{II} ions, we cannot know the orientation of the projection of the field within their hard planes caused by the 15° tilting of the easy axes. Thus, the two sets of curves illustrate the extreme cases corresponding to projection onto the hard and medium directions. One clearly sees that the lack of this information at this stage in the analysis does not dramatically influence our initial estimates of D_i, E_i, *g*, or the easy-axis tilting angle.

Finally, we comment on the selection rules governing the three branches of resonances in Figure 3. First of all, as the sample is rotated in the horizontal field magnet, the relative orientation between the dc and ac magnetic fields (H_0 and H_1, respectively) changes. Although it is possible to imagine a geometry in which H_0 and H_1 remain orthogonal, one cannot hope to achieve such a situation when working on high-order modes of the cavity ($f > 90$ GHz). In addition, although the dc field is very homogeneous, the sample used in this study was rather large (approximate dimensions: 1.5×1.5 mm^2 square base; 2 mm height). Consequently, the H_1 field was not particularly uniform over the volume of the sample (note that $\lambda/2 \approx 0.5$ mm at 350 GHz); that is, its orientation varies from one part of the sample to another. The relative orientations of H_0 and H_1 will also likely vary from one frequency to the next. Therefore, in general, one expects components of H_1 that are both parallel and perpendicular to H_0. Consequently, both $\Delta M_S = \pm 1$ and $\Delta M_S = \pm 2$ double quantum transitions should be expected. Indeed, the relative intensities of the different resonances differ noticeably for different frequencies (see Figure S3 in the Supporting Information). In addition to this, there is strong mixing between the T_y and T_z states in the 3−7 T

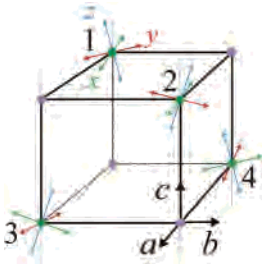

Figure 5. Schematic representation of the four possible principal single-ion magnetic axes (x_i, y_i, z_i) tilted with respect to the crystallographic axes (a, b, c). A solid cube is drawn with each of the edges aligned with the crystal axes to guide the eyes and to show their relationships. We note that the real $[NiZn_3(hmp)_4(dmb)_4Cl_4]$ molecule has a distorted cube structure.

range. This mixing also affects EPR selection rules, thereby allowing transitions that might otherwise be forbidden for a much higher symmetry geometry. It is for this reason that we simply label the three resonance branches *A*, *B*, and *C*; that is, it is meaningless to try to label them in terms of simple quantum numbers. Furthermore, we expect to observe all three resonances for essentially all field orientations and frequencies; that is, no clear selection rules apply.

Single-Ion ZFS. To obtain more precise information concerning the orientations of the magnetic axes associated with the individual Ni^{II} ions, further angle-dependent experiments were performed. Because the orientations of the crystallographic axes can be easily identified from the shape of the crystal, the sample can be manually aligned within the cavity for rotation in a desired crystallographic plane. However, such an alignment is never perfect, and it is, thus, necessary to introduce additional parameters to correct for small misalignments. In general, three parameters (Euler angles: α, β, γ) are required in order to relate any two coordinate systems; these angles are defined in Figure S4 in the Supporting Information and in ref 26. We correct for any misalignment of the sample within the cavity by defining a set of Euler angles C_α, C_β, and C_γ, which relate the crystallographic (*c*) and laboratory (*l*) coordinate frames, that is, (a, b, c) $\leftrightarrow$ (X, Y, Z).

We can now approximate the $[Zn_3Ni(hmp)_4(dmb)_4Cl_4]$ molecule as a cube with its edges aligned with the crystallographic *a*, *b*, and *c* axes, as shown in Figure 5, with four possible positions (labeled 1−4) for the lone Ni^{II} ion. We note that the actual molecule has a distorted cube structure. Next, we must relate each of the four single-ion coordinate frames (x_i, y_i, z_i) with the crystallographic axes (a, b, c); the subscripts *i* refer to the four positions. Because of the 4-fold symmetry of the crystal, only a single set of Euler angles (S_α, S_β, S_γ) is needed to completely specify these four coordinate systems; that is, S_α, S_β, and S_γ specify the single-ion axes at one of the sites (e.g., $i = 1$), and the remaining three are related by the crystallographic symmetry group.

(26) The transition from one coordinate system to the other is achieved by a series of two-dimensional rotations. The rotations are performed about coordinate system axes generated by the previous rotation step. The convention used here is that α is a rotation about the *z* axis of the initial coordinate system. About the y' axis of this newly generated coordinate system, a rotation by β is performed, followed by a rotation by γ about the new *z* axis.

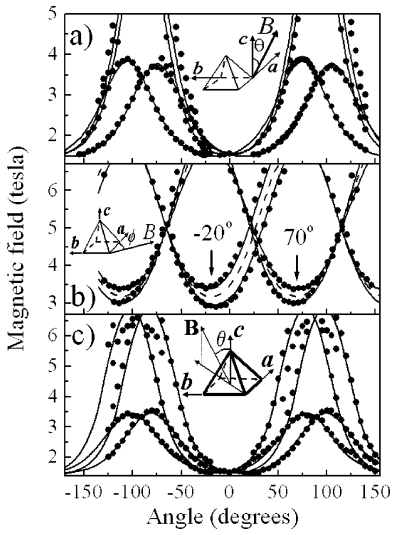

Figure 6. Angle dependence of the EPR peak positions corresponding to resonance *A* (Figure 4) for (a) orientation 1, field rotation approximately in the *ac* plane (or *bc* plane); (b) orientation 2, field rotation approximately in the *ab* plane; and (c) orientation 3, field rotation approximately in the plane containing the (110) and (001) crystallographic directions. The insets depict the experimental geometry. In each case, the temperature was 2.5 K and the frequencies were (a) 119.9 GHz, (b) 122.8 GHz, and (c) 117.7 GHz. The experimental spectra can be observed in the Supporting Information. The solid curves are fits to the data, and the dashed curves in b represent the averages of the pairs of almost degenerate curves (see main text). The directions of the projections of the single-ion hard and medium directions onto the *ab* plane have been indicated in b.

The single-ion axes illustrated in Figure 5 have been oriented approximately as deduced from these studies. For the ensuing discussion, we use the angles θ and ϕ to denote polar angles; we use the subscripts *l* and *c* to refer to the laboratory and crystal coordinate systems, respectively, and subscript *i* (= 1−4) to denote the four single-ion coordinate systems (Figure 5).

Angle-dependent measurements were performed for three separate planes of rotation; the blueprints for the three experiments are illustrated in Figure S5 in the Supporting Information. For orientation 1, we rotated the field approximately in the crystallographic *ac* plane (or the *bc* plane, because it is indistinguishable by symmetry), that is, in a plane parallel to one of the vertical cube faces in Figure 5. For orientation 2, we rotated the field approximately in the crystallographic *ab* plane, that is, in a plane parallel to the horizontal cube faces in Figure 5. Finally, for orientation 3, we rotated the field in a plane approximately intersecting the crystallographic *ac* and *bc* planes, that is, a vertical plane crossing the horizontal diagonals of the cube in Figure 5. These geometries are also depicted as insets to Figure 6. A frequency close to 120 GHz was carefully selected for these experiments. This sits just at the lower edge of a gap between the *B* and *C* resonance branches (Figure 3). In fact, 120 GHz is right at the zfs between the T_y and T_z levels (Figure 4). Consequently, resonance *C* is always observed as a broad absorption at zero field and resonance *B* is always found at higher frequencies. Meanwhile, the position of resonance *A* depends strongly on the field orientation at 120 GHz, moving from 1.5 T upward to the maximum available field of 7 T for field orientations close to the hard magnetic directions.

In this way, 120 GHz provides the lowest frequency (hence, the best signal-to-noise ratio) with which we can focus on the angle dependence of a single resonance; that is, resonances *B* and *C* do not interfere with the angle dependence of resonance *A* over the full 4π radians.

Figure 6 displays the angle dependence of peaks corresponding to resonance *A* (at 2.5 K and $f \approx 120$ GHz) for the three chosen planes of rotation. Representative experimental spectra are displayed in Figure S6 in the Supporting Information, and the precise frequencies are listed in the figure caption. For each plane of rotation, four resonance branches are observed corresponding to the four Ni^{II} sites, thus confirming the earlier conclusion concerning the noncollinearity of the magnetic axes at each site. The solid curves are fits to the data; we describe the fitting procedure in detail below. In parts a and c of Figure 6, the experimental angle ("offset") has been calibrated so that the high-symmetry points occur at $\theta_l = 0°$ and $\theta_l = 90°$. For both of these orientations, the Euler angle $C_\beta \approx 0$. Consequently, the angles θ_l and θ_c are approximately equivalent. Meanwhile, the angle in Figure 6b (orientation 2) is referenced to the approximate orientation of the crystallographic *a* (or *b*) axis, as deduced via microscope images of the sample mounted in the cavity. We estimate the error of this calibration to be $\pm 5°$.

Before discussing the data, we briefly review the Hamiltonian for spin $S = 1$. We can write the Hamiltonian operator in matrix form as follows:

$$\hat{H}_i = \begin{pmatrix} D + \mu_B g_z B \cos(\theta_i) & A_i & E \\ A_i^* & 0 & A_i \\ E & A_i^* & D - \mu_B g_z B \cos(\theta_i) \end{pmatrix}$$

where

$$A_i = 0.707 \mu_B B[g_x \sin(\theta_i) \cos(\phi_i) - i g_x \sin(\theta_i) \sin(\phi_i)] \quad (1)$$

It should be noted that the angles θ_i and ϕ_i involved in this Hamiltonian represent the spherical polar coordinates referenced to each of the individual Ni^{II} spin coordinate frames (x_i, y_i, z_i), as depicted in Figure 5. All other terms in eq 1 represent zfs interactions, which we find to be the same for all four ions. One must then independently transform the lab coordinates into each spin coordinate system using the two Euler transformations described earlier. For each experimental orientation, this involves a separate set of *C* parameters. However, our fitting procedure is designed to obtain a single set of *S* parameters.

The next step involves solving for the eigenvalues (frequencies) for all four spin sites, as a function of the applied magnetic field strength and its orientation. We note that the field was only ever rotated about a single axis for a particular experiment; thus, the field strength (*B*), and its orientation (θ_l) in the lab frame, represent the only variables in this procedure. Upon doing so, we obtain four 3D surfaces (frequency, field, orientation), one for each Ni^{II} site. For rotations in high-symmetry crystallographic planes, the number of surfaces may be reduced because of degeneracies. However, we shall see that, in general, the experimental geometry was such that these degeneracies are completely lifted. Figure 7 shows a pair of doubly degenerate surfaces for rotation exactly in the *ab* plane, that is, very close to the rotation plane for orientation 2 (Figure 6b). We then perform a "virtual" experiment, where we pick a measurement frequency (*f*) and solve for the intersection between the constant *f* surface and the four 3D surfaces. The resulting curves describe the angle dependence of the spectra for a particular set of *C*, *S*, and zfs parameters (D_i, E_i, and *g*). The final and most complicated task involves performing a least-squares fit to the full data set (orientations 1−3).

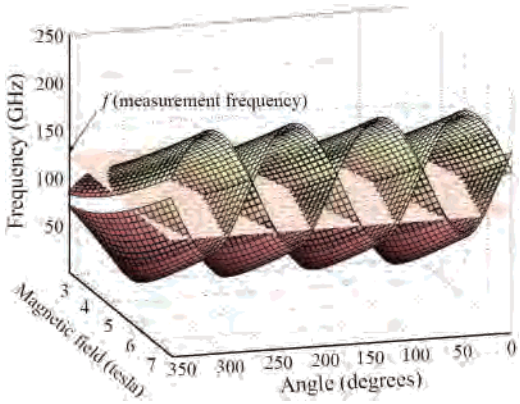

Figure 7. Simulated resonance surfaces for field rotation exactly in the *ab* plane. Two branches of resonances are seen (see the main text for an explanation). The angle dependence of the resonance positions is found via the intersection of the surfaces with a horizontal plane corresponding to the experimental measurement frequency. The simulations assume the parameters given in Figure 4.

As already noted, the four resonance branches seen in Figure 6 originate from each of the four Ni^{II} sites (Figure 5). All degeneracies were avoided because of small misalignments of the sample within the cavity for each rotation plane, that is, finite *C* parameters (Euler angles). However, it is apparent that this alignment was fairly good in the case of orientation 1, because the two high-field branches are almost degenerate. In zero magnetic field, the magnetic dipole transitions for all four Ni^{II} ions must be degenerate because of the symmetry equivalence of the four sites. Application of a magnetic field breaks this symmetry. However, a magnetic field along the *c* axis will not lift any degeneracies because of the axial symmetry, whereas a field applied within the *ab* plane will only partially lift the 4-fold degeneracy; that is, in general, the spectrum will split into two branches, as illustrated in Figure 7. Note that the curves for orientations 1 and 3 (Figure 6a,c) intersect at a single point at $\theta_l = 0°$ ($\approx \theta_c$) and at two points for $\theta_l = 90°$. The two branches arise because of the *E* term; when the field is roughly parallel to the x_i axes of two of the ions, it must be approximately orthogonal to the x_i axes of the other two. Thus, it is the combination of the Zeeman and *E* terms that lifts the degeneracy.

As soon as the field is tilted away from either the *c* axis, or the *ab* plane, the degeneracy will, in general, be completely lifted. This is why four branches are seen for each experiment. In particular, for orientation 2, the rotation plane was inclined at an angle $C_\beta = 9.8°$ away from the *ab* plane, causing the splitting of the two main branches. The dashed curves in Figure 6b reveal the average behavior of

each split branch. The minima of the dashed curves, which are separated by exactly 90° (as required by symmetry), correspond to the directions of the projections of the medium axes of the individual Ni^{II} ions (y_i) onto the *ab* plane. Meanwhile, the projections of the hard axes (x_i) correspond to the maxima in the dashed curves (not shown in Figure 6b) that, to within the experimental resolution, occur at the same angles. Thus, from Figure 6b, we can conclude that the hard and medium axes of the Ni^{II} ions (x_i and y_i) project onto the *ab* plane along directions given by $\phi_c = 70 \pm 5° + (n90°)$ (n = integer) relative to the *a* axis; the ±5° results from the uncertainty in the alignment of the crystal within the cavity.

On the basis of the near degeneracy of the two high-field branches seen for orientation 1 (Figure 6a), one can conclude that the single-ion easy axes tilt approximately along the crystallographic *a* and *b* directions (±5°), that is, $S_\alpha \approx 0°$, 90°, and so forth. It is, then, straightforward to deduce the single-ion easy-axis tilting angle (S_β) from the separation of the low-field (~3.75 T) maxima in Figure 6a. This maximum separation of 30 ± 1° corresponds to the angle between hard planes associated with Ni^{II} sites that are related by a 180° rotation (see Figure 5), implying that the easy axes for each Ni^{II} ion are tilted 15 ± 0.5° ($= S_\beta$) away from the *c* axis, as previously inferred on the basis of the frequency dependence. Finally, we can conclude from the low-field maxima in Figure 6a that the magnetic field intersects the hard planes associated with the two Ni^{II} ions responsible for these maxima closer to their medium directions (~20° away) than their hard directions. Thus, on the basis of the discussion of Figure 6b above, we infer that the Euler angle $S_\gamma = 70 \pm 5°$ (or 250 ± 5°) for the ions with $S_\alpha \approx 0°$ (or 180°) and $S_\gamma = 160 \pm 5°$ (or $-20 \pm 5°$) for the ions with $S_\alpha \approx 90°$ (or 270°). For a more detailed explanation, refer to the Supporting Information.

The optimum single-ion zfs parameters obtained from these angle-dependent measurements, as well as frequency-dependent studies performed with the magnetic field applied along the crystallographic *c* axis (Figure 3), and the *a*/*b* axes (not shown), yield $D_i = -5.30(5)\ cm^{-1}$, $E_i = \pm 1.20(2)\ cm^{-1}$, $g_z = 2.30(5)$, and $g_x = g_y = 2.20(5)$. To within our experimental accuracy, the obtained *g* anisotropy is marginal. On the basis of the obtained D_i and E_i values, one would expect a difference between g_z and g_{xy} [$= {}^1/_2(g_x + g_y)$] on the order of 0.02 and a difference between g_x and g_y on the order of 0.01.[22] This is *not* inconsistent with the obtained values. Unfortunately, the relatively broad EPR signals do not permit a more precise determination of the *g* anisotropy.

Temperature Dependence. We conclude this section by examining the temperature dependence of the *A* resonance. Figure 8 displays data obtained at temperatures between 2.5 and 10 K, at a frequency of 119.9 GHz; the field is oriented approximately along the *c* axis of the crystal. The inset to Figure 8 shows the energy level diagram for $S = 1$, with a negative uniaxial D_i [$= -5.30(5)\ cm^{-1}$] parameter [also, $E_i = \pm 1.20(2)\ cm^{-1}$]. As can be seen from the figure, the *A* transition occurs from the ground state. Thus, one should expect the intensity of this transition to increase as the temperature is decreased. This is precisely the behavior seen in the main part of Figure 8. In contrast, if the sign of D_i was positive, the energy level diagram would be inverted. In this case, the *A* transition would occur from an excited state and its intensity should decrease at the lowest temperatures. Because such behavior is not observed, we can conclude from the temperature-dependent studies that the sign of D_i must be negative.

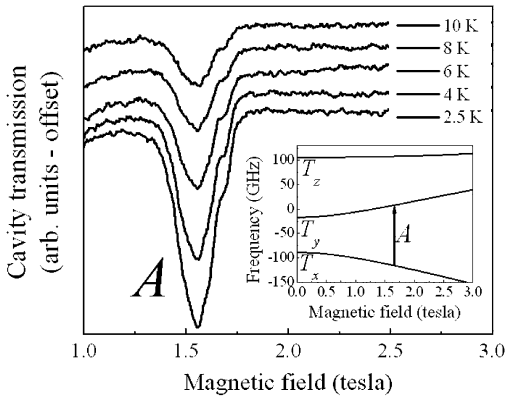

Figure 8. Temperature dependence of the *A* resonance between 2.5 and 10 K and at a frequency of 119.9 GHz; the field is oriented approximately along the crystallographic *c* axis. The inset shows the energy level diagram for $S = 1$, with a negative uniaxial D [$= -0.530(5)\ cm^{-1}$] parameter [also, $E = \pm 1.20(2)\ cm^{-1}$]. As can bee seen from the figure, the *A* transition occurs from the ground state.

ZFS of the $S = 4$ Ground State of the Ni_4 SMM. The SMM complex $[Ni_4(hmp)_4(dmb)_4Cl_4]$ has a spin $S = 4$ ground state as a result of the ferromagnetic coupling of the four Ni^{II} ions. The barrier for magnetization reversal is approximately equal to $S^2|D|$, where D gauges the axial zfs, $D\hat{S}_z^2$, in the $S = 4$ ground state. In this section, it is shown how the single-ion zfs interaction for the single Ni^{II} ion in the $[Zn_3Ni(hmp)_4(dmb)_4Cl_4]$ molecule doped into the lattice of diamagnetic Zn^{II}_4 molecules gives rise to the axial zfs interaction for the $S = 4$ ground state of the Ni^{II}_4 SMM.

In the previous section, the zfs parameters for the Ni^{II} ion in $[Zn_3Ni(hmp)_4(dmb)_4Cl_4]$ were evaluated by HFEPR to be $D_i = -5.30(5)\ cm^{-1}$ and $E_i = \pm 1.20(2)\ cm^{-1}$. The zfs matrix in each local Ni^{II} coordinate system is of the form

$$\overline{\overline{D}}_{local} = \begin{bmatrix} -D_i/3 + E_i & 0 & 0 \\ 0 & -D_i/3 - E_i & 0 \\ 0 & 0 & 2D_i/3 \end{bmatrix} \qquad (2)$$

Hereafter, the double bar symbol above each capital letter represents a 3 × 3 matrix. This matrix has to be converted from the local coordinate framework to the crystal lattice coordinate framework. This transformation is made by means of the Euler matrix $\overline{\overline{A}}$, where the Euler angles S_α, S_β, and $S_\gamma = 0°$, 15°, and 70°, respectively, and is given as

$$\overline{\overline{D}}_{crystal} = \overline{\overline{A}}^{-1}\overline{\overline{D}}_{local}\overline{\overline{A}} \qquad (3)$$

In the Ni_4 complex, there are four Ni^{II} ions, and if we define $\overline{\overline{D}}_1 \equiv \overline{\overline{D}}_{crystal}$ for Ni^{II} ion number 1, then the total zfs matrix for a Ni^{II}_4 molecule is given by eq 4.

$$\overline{\overline{D}}_{\text{total}} = d_1\overline{\overline{D}}_1 + d_2\overline{\overline{D}}_2 + d_3\overline{\overline{D}}_3 + d_4\overline{\overline{D}}_4 + d_{1,2}\overline{\overline{D}}_{1,2} + d_{1,3}\overline{\overline{D}}_{1,3} + d_{1,4}\overline{\overline{D}}_{1,4} + d_{2,3}\overline{\overline{D}}_{2,3} + d_{2,4}\overline{\overline{D}}_{2,4} + d_{3,4}\overline{\overline{D}}_{3,4} \quad (4)$$

In this equation, $\overline{\overline{D}}_i$ ($i = 1, 2, 3, 4$) represents the zfs matrices for the individual ions, $\overline{\overline{D}}_{i,j}$ ($i, j = 1, 2, 3, 4$) represents the asymmetric dipolar couplings between metal centers i and j, and d_i and $d_{i,j}$ are their expansion coefficients. The values of d_i and $d_{i,j}$ are calculated by irreducible tensor methods.[27−29] In the Ni^{II}_4 cubane molecule, $S_1 = S_2 = S_3 = S_4 = 1$ and $S = 4$. Thus,

$$\overline{\overline{D}}_{\text{total}} = {}^1/_{28}\overline{\overline{D}}_1 + {}^1/_{28}\overline{\overline{D}}_2 + {}^1/_{28}\overline{\overline{D}}_3 + {}^1/_{28}\overline{\overline{D}}_4 + {}^2/_{28}\overline{\overline{D}}_{1,2} + {}^2/_{28}\overline{\overline{D}}_{1,3} + {}^2/_{28}\overline{\overline{D}}_{1,4} + {}^2/_{28}\overline{\overline{D}}_{2,3} + {}^2/_{28}\overline{\overline{D}}_{2,4} + {}^2/_{28}\overline{\overline{D}}_{3,4} \quad (5)$$

Because the $\overline{\overline{D}}_{i,j}$ values are mainly from dipole−dipole interactions, for simplicity, we ignore their contribution to $\overline{\overline{D}}_{\text{total}}$. This is reasonable because the $\overline{\overline{D}}_{i,j}$ values are on the order of 0.1 cm^{-1}, whereas in the Ni^{II}_4 complex **3**, $\overline{\overline{D}}_1$ is about 5 cm^{-1}. This gives eq 6:

$$\overline{\overline{D}}_{\text{total}} = {}^1/_{28}\overline{\overline{D}}_1 + {}^1/_{28}\overline{\overline{D}}_2 + {}^1/_{28}\overline{\overline{D}}_3 + {}^1/_{28}\overline{\overline{D}}_4 \quad (6)$$

The $\overline{\overline{D}}_i$ matrices for the other three Ni^{II} ions numbered 2, 3, and 4 can be related to $\overline{\overline{D}}_1$ for Ni^{II} ion number 1 by employing the matrix for the S_4 symmetry operation. The transformations for $\overline{\overline{D}}_2$, $\overline{\overline{D}}_3$, and $\overline{\overline{D}}_4$ are then given by eq 7: The numerical results for $\overline{\overline{D}}_{\text{total}}$, with the positive single-ion

$$\begin{aligned}\overline{\overline{D}}_2 &= \overline{\overline{S}}_4{}^1\overline{\overline{D}}_1\overline{\overline{S}}_4{}^{-1}\\ \overline{\overline{D}}_3 &= \overline{\overline{S}}_4{}^2\overline{\overline{D}}_1\overline{\overline{S}}_4{}^{-2}\\ \overline{\overline{D}}_4 &= \overline{\overline{S}}_4{}^3\overline{\overline{D}}_1\overline{\overline{S}}_4{}^{-3}\end{aligned} \quad (7)$$

E_i value, are given as follows (in GHz):

$$\overline{\overline{D}}_{\text{total}} = \begin{bmatrix} 6.8998 & 0 & 0 \\ 0 & 6.8998 & 0 \\ 0 & 0 & -13.7995 \end{bmatrix} \quad (8)$$

It is satisfying that $\overline{\overline{D}}_{\text{total}}$ is a traceless diagonal matrix with (1, 1) = (2, 2). From eq 2, this implies that $E = 0$ for the $S = 4$ ground state of the Ni^{II}_4 SMM, as expected for this complex, which has S_4 site symmetry, requiring that $E = 0$. From eqs 2 and 8, we can calculate that $D = -0.69$ cm^{-1} for the positive single-ion E_i value (and $D = -0.66$ cm^{-1} for a negative single-ion E_i value) for the $S = 4$ ground state. Given the approximations made in this calculation, agreement with the experimentally determined D value of -0.600 cm^{-1} is remarkably good.

Origin and Importance of ZFS for the $S = 4$ Ground State of the Ni^{II}_4 SMM. It was shown in the last section how the single-ion zfs interactions at each metal ion site contribute to the zfs interaction for the ground state of a SMM. For metal ions such as Ni^{II} that have an orbitally nondegenerate ground state in a low-symmetry coordination site, the origin of the zfs interaction is the admixture of excited states into the ground-state wave function that result from spin−orbit coupling ($\lambda\hat{L}\hat{S}$). These single-ion zfs effects are parametrized in a spin Hamiltonian with terms such as $D_i\hat{S}_z^2$ and $E_i(\hat{S}_x^2 - \hat{S}_y^2)$, the axial and rhombic zfs interactions. Here, we retain the subscript i to distinguish between single-ion and SMM zfs parameters. The magnitude and sign of the D_i parameter (and of the E_i parameter) depend on the magnitude and sign of the spin−orbit coupling constant λ and on how close in energy the excited states are that are spin−orbit admixed with the ground state. The single-ion D_i value for a Ni^{II} complex has been found to be positive in some complexes but negative in others.[21,22] For six-coordinate Ni^{II} complexes with six equivalent ligands, D_i values have been reported in the range of -3.05 to $+1.70$ cm^{-1}. In a recent paper,[30] Krzystek et al. used HFEPR to determine $D_i = +13.20(5)$ cm^{-1} for the four-coordinate tetrahedral Ni^{II} complex $Ni(PPh_3)_2Cl_2$; the complex $Ni(PPh_3)_2Br_2$ gave $D_i = +4.5(5)$ cm^{-1}. Thus, four-coordinate complexes generally have larger $|D_i|$ values than do six-coordinate complexes, because the excited states are closer in energy to the ground state in the case of the former. Consequently, the magnitude and sign of D_i for a Ni^{II} complex reflects the number and geometry of the ligands. In addition, the orientations of the principal magnetic axes associated with the single-ion zfs interaction reflect the positioning of the ligand atoms. In other words, the z_i direction associated with the $D_i\hat{S}_z^2$ axial zfs interaction might correspond to a metal−ligand bond direction, or some other orientation depending on the positioning and symmetry of the ligands. The magnitude, sign, and direction of the single-ion zfs interaction ultimately determine the zfs interaction in a Ni^{II}_4 SMM. If the D_i value for a Ni^{II} ion is negative, then it is necessary that the magnetic z_i axis of that ion not be inclined too far away from the magnetic z axis of the Ni^{II}_4 SMM (c axis in this case). Alternatively, the single ion D_i value could be positive. However, in this situation, the single-ion magnetic z_i axis should be oriented close to the hard plane (xy plane) in order for the positive D_i value to project a negative contribution to the D value for the Ni^{II}_4 SMM.

There are two important ways in which the single-ion zfs interactions (both D_i and E_i) affect the low-temperature magnetization dynamics of a SMM. In order for a SMM to have a potential energy barrier for magnetization reversal, the SMM must have a negative D value. The Ni^{II}_4 SMMs have spin $S = 4$ and the barrier height U_{eff} is $S^2|D| \approx 10$ cm^{-1}. One way for the Ni^{II}_4 SMM to reverse its magnetization direction from "spin-up" ($M_S = -4$) to "spin-down" ($M_S = +4$) is via classical thermal activation over this barrier. Thus, it is clear that the barrier height will affect

(27) Bencini, A.; Gatteschi, D. *Electron Paramagnetic Resonance of Exchange Coupled Systems*; Springer-Verlag: New York, 1990.
(28) Gatteschi, D.; Sorace, L. *J. Solid State Chem.* **2001**, *159* (2), 253−261.
(29) Boca, R. *Theoretical Foundations of Molecular Magnetism*; Elsevier: New York, 1999.
(30) Krzystek, J.; Park, J. H.; Meisel, M. W.; Hitchman, M. A.; Stratemeier, H.; Brunel, L. C.; Telser, J. *Inorg. Chem.* **2002**, *41* (17), 4478−4487.

the low-temperature ($k_BT < S^2|D|$) magnetization dynamics. This barrier height is ultimately related to the tensor projection of the single-ion zfs parameters D_i and E_i.

The single-ion zfs interaction can play an even more important role in determining the quantum (as opposed to classical) magnetization dynamics of a Ni^{II}_4 SMM. At very low temperatures ($k_BT \ll S^2|D|$), where SMMs exhibit blocking of their magnetization, quantum tunneling may become the dominant mechanism of magnetization reversal. In this case, one observes a temperature-independent magnetization relaxation rate, involving tunneling between the $M_s = -4$ and $M_S = +4$ ground states. Transverse interactions in the spin Hamiltonian (terms that do not commute with $\hat{S}_z$) cause this tunneling at a rate which is governed by the tunnel-splitting interaction (raised to some power) which lifts the degeneracy between the $M_S = -4$ and $M_S = +4$ states. How effective this interaction is at causing tunneling depends very sensitively on the symmetry of the spin Hamiltonian and on the magnitude of the spin. Transverse interactions can arise from transverse internal or external magnetic fields (i.e., fields with components in the *xy* plane of the SMM) or from zfs interactions that contain the operators $\hat{S}_x$ and $\hat{S}_y$. As we will show in a later paper, where HFEPR data are presented for a single-crystal of a Ni^{II}_4 SMM, the quartic zfs interaction $B^4_4\hat{O}^4_4$ causes rapid magnetization tunneling. It has been determined in this paper that the Ni^{II} ion easy axes are tilted 15° away from the crystallographic *c* axis (i.e., the molecular easy axis) for the $S = 4$ ground state of the Ni_4 SMM. A significant E_i term is also found for the single Ni^{II} ion. We believe that these factors, when combined with the 4-fold symmetry, project a large B^4_4 term for the $S = 4$ ground state. It will be shown in the later paper exactly how this transverse fourth-order $B^4_4\hat{O}^4_4$ term leads to fast ground-state quantum magnetization tunneling in the Ni_4 SMM. In summary, the single-ion zfs interactions in a Ni^{II}_4 SMM determine both the potential-energy barrier for magnetization reversal and, more importantly, the rate of magnetization tunneling.

Acknowledgment. This work was supported by the National Science Foundation (Grants CHE0095031, CHE0350615, DMR0103290, and DMR0239481).

Supporting Information Available: X-ray crystallographic files in CIF format are available for complexes **1**. Additional figures and tables and a supplementary discussion of the angle-dependent data cited in this paper are also available. This material is available free of charge via the Internet at http://pubs.acs.org.

IC0482279